Computational Materials Science 200 (2021) 110807

Contents lists available at ScienceDirect

Computational Materials Science

journal homepage: www.elsevier.com/locate/commatsci

Understanding defect structures in nanoscale metal additive manufacturing via molecular dynamics

Gurmeet Singh, Anthony M. Waas, Veera Sundararaghavan *

Department of Aerospace Engineering, University of Michigan, Ann Arbor, MI, 48109, USA

ARTICLE INFO

Keywords:
Metal additive manufacturing
Molecular dynamics simulations
Process-structure relationship
Defects evolution
Alloy inclusions

ABSTRACT

Additive manufacturing of a single crystalline metallic column at nanoscale is studied using molecular dynamics simulations. In the model, a melt pool is incrementally added and cooled to a target temperature under isobaric conditions to build a metallic column from the bottom up. The polyhedral template matching (PTM) is used to observe the evolution of atomic-scale defects during this process. The solidification is seen to proceed in two directions for an added molten layer. The molten layer in contact with the cooler lattice has a fast solidification front that competes with the slower solidification front that starts from the top of the melt layer. The defect structure formed strongly depends on the speed of the two competing solidification fronts. Up to a critical layer thickness, the defect-free single crystals are obtained as the faster solidification front reaches the top of the melt pool before the initiation of the slower front from the top. A slower cooling rate leads to a reduction in defects, however, the benefits diminish below a critical rate. The defect content can be significantly reduced by raising the temperature of the powder bed to a critical temperature. This temperature is governed by two competing mechanisms: the slower cooling rates at higher temperatures and the increase in amorphousness as one gets closer to the melting point of the metal. Finally, the effect of an added soft inclusion (SiS_2) and a hard inclusion (SiC) on the defect structures is explored. The hard inclusion leads to a retained defect structure while soft inclusions reduce defective content compared to the pure metal.

1. Introduction

Additive manufacturing (AM) is now being routinely used in industry to build metal parts due to the flexibility it allows in part design. Additive manufacturing involves a gradual increase in the size and shape of solids due to the addition of new layers of the material on top of the existing ones. Thermally enabled metal additive manufacturing (MAM) consists of fast heating (e.g. using lasers) of the powder beds leading to large thermal gradients followed by high cooling rates due to the small volumes that are exposed at a time [1,2]. A resolution of up to 20 μm per layer [3] and components with functionally graded materials has been realized [4]. The defect formation during additive manufacturing is a subject of ongoing in-depth studies as it relates to the accelerated fatigue and fracture of a manufactured part [5]. There is a high dependence on several processing parameters which dictates the mechanism and properties of the final product [2,6–8]. Wang et al. studied the influence of both the laser scan rate and laser power on the residual stresses in the fabricated samples [9,10]. Their findings revealed that higher laser power led to an increase in the residual stress in the build direction and laser speed influences the stresses in transverse directions of the additive sample [10]. Fig. 1 shows a schematic of the metal additive manufacturing process (center) with a resulting representative microstructure.

To understand the microstructure evolution and defect formation as a function of process parameters, it is important to comprehend solidification processes in the melt and how it influences the defect structure in an additive column. Several simulation methods have been applied to study the solidification phenomenon at different scales [11,12]. Cellular automata in conjunction with temperature history from a finite element analysis (FEA) [13], finite volume [14], or finite difference solutions [15] have been implemented to predict the grain size and texture during solidification under arc welding or additive manufacturing process. A continuum scale model by Prabhakar et al. [16] was implemented that employs FEA and thermal history to simulate the deformation and distortion of the part. Another popular choice for simulating structure at meso scales is phase-field (PF) modeling [17,18]. However, because of the length scale and extreme heating and cooling rates, melt solidification is a highly non-equilibrium process and continuum methods alone are not sufficient.

* Corresponding author.
E-mail address: veeras@umich.edu (V. Sundararaghavan).

https://doi.org/10.1016/j.commatsci.2021.110807
Received 22 March 2021; Received in revised form 21 July 2021; Accepted 12 August 2021
Available online 2 September 2021

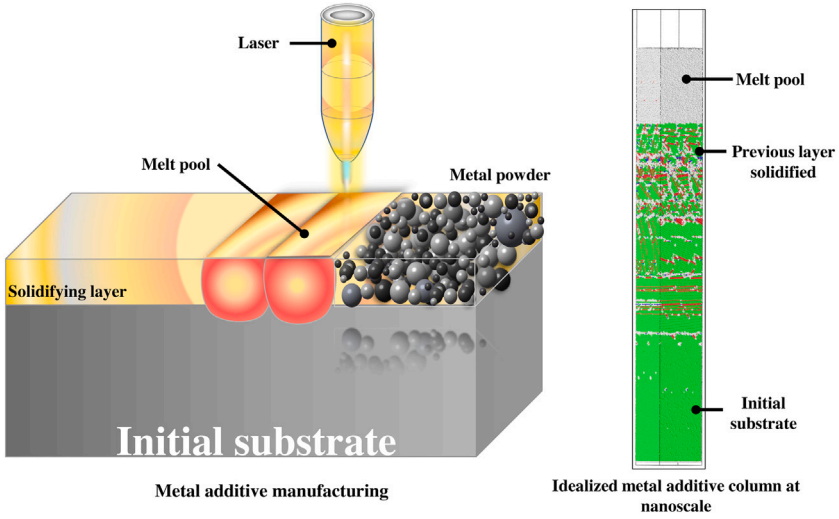

Fig. 1. A schematic of the additive manufacturing process (left) and the idealized additive process at the nanoscale (right).

Molecular dynamics simulations can capture the non-equilibrium physics by efficiently representing the inter-atomic interactions during solidification using the well-calibrated interatomic potentials. Although only small volumes (nanoscale) can be simulated, such simulations have allowed prediction of bulk phenomena in the past including the understanding of metal curves [19,20], nucleation and grain growth [21], solidification defects [22,23], and the vacancy formation during solidification [24]. Kurian et al. [25] recently employed large-scale molecular dynamics simulations to study the melt behavior and its interaction with nano-powdered particles and subsequent solidification. This study showed the process of crystal nucleation in the melt and the emergence of grain boundaries as well as voids during the process. Another study by Jiang et al. [26] employed molecular dynamics simulations to understand the crystallization and cluster evolution patterns for various laser powers and scan rates in $Fe_{50}Ni_{50}$ amorphous alloy. These investigations demonstrated that the low scanning speeds allow increased crystallization into body-centered cubic (BCC) structure. Furthermore, the low energy density of the laser diminishes crystallization and leads to a more amorphous structure [26]. However, a detailed account of atomic-scale defects as a function of process parameters was not performed in these studies, and this is the goal of the current work.

During the solidification of grains, various defect structures form that are either unstable (e.g. self-interstitial) which are relieved during reheating, or more stable defect structures (e.g. high angle grain boundaries) that persist after the process. Understanding the formation of defects as a function of parameters such as cooling rates, particle bed temperature, presence of inclusions, etc. has not yet been carried out via molecular simulations. Hu et al. have experimentally studied the effect of cooling rates on the microstructural characteristics in a MAM process [27] and found that fast cooling rates result in small grain size and at the slower cooling rates, large grain structures were observed. There have also been experimental investigations on the effect of layer thickness by Sui et al. [28], and on the influence of substrate temperature (preheated bed) [29] on the microstructure evolution and its mechanical performance [7]. By increasing the substrate temperature to 1000 °C, mitigation in the extent of the microcrack density was observed in Tungsten as compared to preheated bed at 200 °C. In this study, we analyze the effect of such process parameters by idealizing an additive column at the nanoscale using molecular dynamics (MD) as shown in Fig. 1 (right). Fundamental reasons for these effects are analyzed and interpreted at the atomistic scale.

In this work, we model the melting and cooling of successive layers of the material. The simulations idealize the process at nanoscale and the metallic column simulated in this work, in the context of nanoscale additive process (shown in Fig. 1(right)). Because of the length and time scale limitations of molecular dynamics, we consider this approach as geared towards investigating defect mechanisms in a corresponding 3D printed nanoscale material rather than conventional metal additive manufacturing. Additionally, the simulation set-up is specific to capturing layer-to-layer interactions, rather than track-to-track interactions (seen in Fig. 1(left)) across meltpools . To simulate this process, we first obtain the equilibrated density of the liquid metal at a temperature above the melting point. A liquid melt of this density is then poured onto a solidified substrate in a layer-by-layer fashion along the build direction (we choose ⟨001⟩ for both Cu and Al systems) followed by cooling down the system to a target temperature. The study primarily aims to understand the defect structure and its origin as a function of several process variables such as cooling rates, layer thickness, and bed temperature from an atomistic viewpoint. Section 3 presents a detailed discussion of the phenomena that leads to the differentiation of single crystals into dislocation defects or amorphous regions as a function of these process variables. In the latter part of the section, we simulate the effect of inclusions in the melt on the resulting defect structure. Section 4 presents the key conclusions drawn from this study.

2. Methods

All MD simulations are performed using the large-scale atomic/molecular massively parallel simulator (LAMMPS) [30]. A supercell of copper of user-specified dimensions is generated as the basis for an initial solid seed region with periodicity in all directions. The supercell is initially equilibrated to a target bed temperature (T_{cool}) using NPT simulation that employed an Andersen barostat [31] at atmospheric pressure and a Nosé–Hoover (NH) thermostat [32]. The Andersen barostat only allows isotropic changes to the unit cell and ensures that the FCC lattice has the correct equilibrium volume at room temperature. To estimate the density of the liquid (ρ_{liquid}) at the melting temperature, this cell is heated to T_{liquid} using another NPT simulation. The liquid cell density is noted and subsequently used while adding liquid layers during the additive process.

During the deposition simulation, the following process is followed (shown in Fig. 2). The equilibrated supercell (at T_{cool}) of a known thickness (t) is initialized at a target temperature (T_{cool}) and a vacuum layer is created on top. At each deposition stage, the same volume as the solid supercell is amorphously packed at the top of the solid column at the liquid density ρ_{liquid} estimated previously. The solid atoms are then fixed and an NVT simulation is used to equilibrate the liquid layer to the melt temperature (T_{liquid}) using velocity re-scaling. The solid atoms

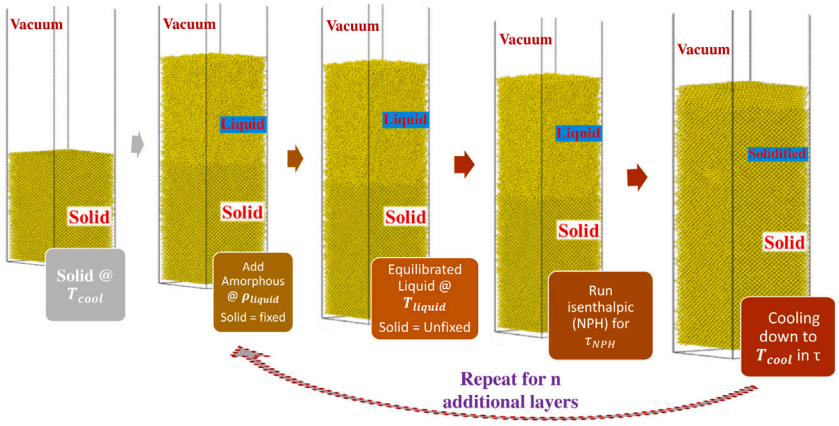

Fig. 2. Steps for molecular dynamics simulation of the additive manufacturing process.

are then unfixed and the system is run under constant enthalpic (NPH) step to simulate interaction of the molten layer with the substrate allowing remelting of the substrate layers. This step is performed for a duration of $\tau_{NPH} = 5$ ps within which the isenthalpic interaction leads to remelting in the substrate layers without any solidification. This is followed by a cool-down starting from the equilibrated velocities using the NH thermostat and an Andersen barostat at atmospheric pressure. Along the build direction, a vacuum region is maintained to avoid self-interactions along the build axis. The entire cell is cooled back to a set temperature (T_{cool}) over a specified time (τ). Once cooled back to T_{cool}, the melt layer equilibrates approximately to a layer thickness (t) accounting for contraction during cooling. In the next deposition stage (for the second melt pool), the process is repeated by amorphously packing another liquid layer at the top of the newly solidified structure at the known liquid density ρ_{liquid} and repeating the cooling steps detailed above.

The layer thickness and cooling time can be controlled in the simulation. Higher substrate temperatures (use of preheated beds) can be simulated by changing the equilibration temperatures set for the thermostat. For an exhaustive account, the effect of the following parameters are investigated in this work:

- Cooling time (τ) of each deposited layer
- Thickness of deposited layers (t)
- Target cooling temperature (T_{cool}) of each deposited layer
- Influence of a soft (SiS_2) and hard (SiC) inclusion in each deposited layer

The structure type in the simulation box is identified by performing the polyhedral template matching (PTM) [33] in Ovito [34,35], an open-source visualization tool. PTM is preferred over conventional common neighbor analysis (CNA) [36] due to its ability to classify the atomic configurations even at elevated temperatures near the melting point. The root mean square (RMS) error cutoff of 0.14 is used for the PTM analysis. Since FCC metals are chosen in this study, we refer to the FCC content in the lattice as the defect-free content for the additive column. In the perfect FCC crystal lattice, three equivalent close-packed planes are aligned along the ⟨111⟩ direction, which leads to an atomic stacking sequence of the form ABCABCABC. A typical defect is the formation of a stacking fault, which occurs when the stacking sequence changes through removal or misalignment of one of the layers in the form ABCABABC. Such regions are identified to be of hexagonal close-packed (HCP) form in the software. The higher energy crystal structures of the body centered cubic (BCC) form are also identified. The clusters that do not fall under the classification of cubic or hexagonal crystals are termed 'amorphous' and may contain defects such as grain boundary dislocations, shockley partials, vacancies, and self-interstitial in addition to disordered clusters. The actual nature

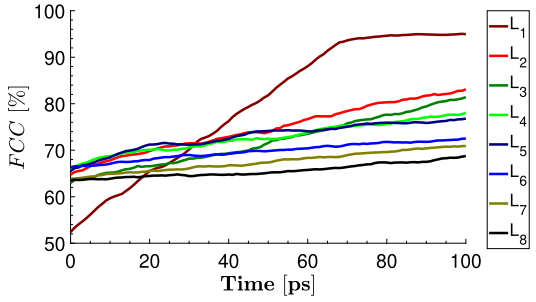

Fig. 3. Evolution of FCC structure with cooling time for $16a \times 16a \times 32a$ system.

of these amorphous defects is obtained through observation. These clusters are identified at the end of the cooling time for each layer. After an ith layer is added to the additive column, the percentage of each structure is computed at layer number L_i using the following equation:

$$\%FCC^i = \frac{N^i_{FCC}}{N^i_{total}} \times 100 \quad \text{and} \quad \%Amorphous^i = \frac{N^i_{Amorphous}}{N^i_{total}} \times 100 \qquad (1)$$

where, we refer to $i = 0$ as the initial solid crystal and for $i = 1$ as the first liquid layer (L_1) added and so on. N^i_{FCC}, $N^i_{Amorphous}$ and N^i_{total} are the number of FCC atoms, amorphous atoms and total number of atoms after the ith layer is added to the additive column, respectively.

3. Results and discussion

The molecular dynamics simulations in these examples are carried out for face-centered cubic (FCC) copper (melting point of 1358 K) using an embedded atom model (EAM) potential describing the atomic interactions [37]. The lattice constant of copper is $a = 3.597$ Å at $T_{cool} = 300$ K. The melt is heated to 1500 K and at this temperature, the density is computed as $\rho_{liquid} = 7.8$ gcm^{-3}. Each liquid layer is equilibrated at $T_{liquid} = 1500$ K for 25 ps before adding to the solidified column. The size ($x \times y \times z$) of the initial supercell considered in this case is $16a \times 16a \times 32a$, with the last number indicating the thickness (t) along the build direction (z). Fig. 3 shows the evolution of FCC content (as given by Eq. (1)) for each added molten layer during cooling within a time of 50 ps. Eight layers in total are simulated. Initial FCC content is low due to the amorphous nature of the liquid melt but tends to increase as the system solidifies to a crystalline structure at room temperature.

Fig. 3 shows that the first melt layer solidifies rapidly (within 60 ps) from the defect-free substrate, but locks in around 5% defects. The subsequent layers take more and more time to achieve a stable defect profile. This is related to the decrease in solidification front speeds

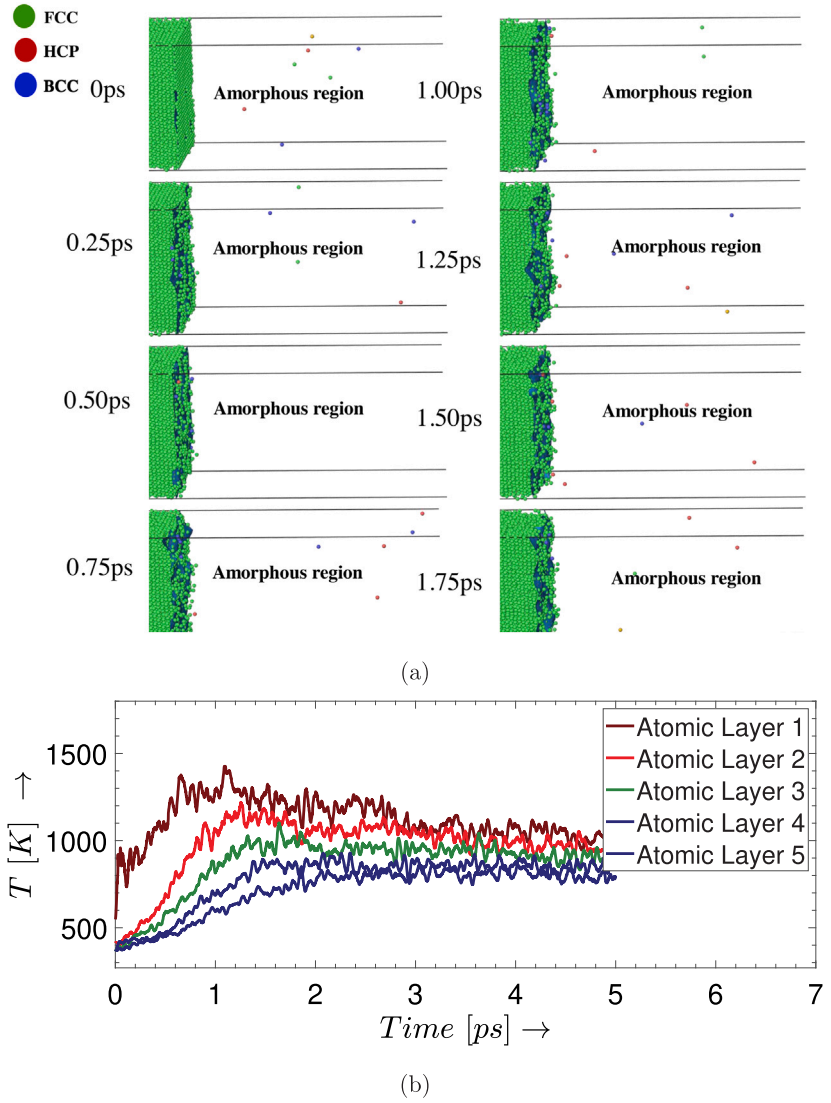

Fig. 4. (a) Remelting of the interface under constant NPH step and (b) temperature vs. time for top five atomic layers of the solid underneath under constant NPH step.

as the defects in the substrate increase, which is studied later in this section. As molten layer 2 is added and equilibrated, some of the defects in layer 1 are ameliorated (see animation01 in SI). However, the defect volume fraction continues to increase from layer 3 onwards due to a lack of sufficient cooling time to eliminate defects. Fig. 4(b) shows the temperature profile of a few atomic layers in the solidified part at the interface. The remelting step is very quick and the remelted layers solidify pretty quickly as the heat flows to the solid part under NPH step. There are 2–3 layers that remelt at the interface. It is observed that remelting is uniform for top 2 layers at the interface as can be seen in Fig. 4(a), however, further layers show non-uniform remelting in their cross sections. The temperature profile for atomic layers 3–5 show that it does not reach the melting point of Cu and the temperature is computed as an average for the atomic layer that have some non-melted portion in it.

Fig. 5 presents this effect of cooling time on the defects in detail. For the 50 ps cooling time detailed previously, the number of defects increases with the number of layers. However, as the cooling time given to the melt is raised to 100 ps, the defect volume fraction significantly reduces with an increase in the number of layers due to sufficient time given for rearrangement and the elimination of higher energy defects. Nevertheless, the slow cooling benefits are lost after 500 ps as the resultant defects are stable and cannot be removed even if the cooling time is increased to 1000 ps (see animation02 for 500 ps case in SI). At 1000 ps cooling time, the percentage of defect-free content converges towards 98% as the number of layers is increased.

3.1. Influence of layer thickness on defects

In this parametric study, the thickness of the melt region is increased keeping the orthogonal dimensions fixed. This simulates larger volumes of molten material added at each step, corresponding to higher energy processing, which affects the solidification kinetics in the build direction (z-axis). The number of atoms in the initial solid and for the liquid layer for four of the thicknesses studied here is presented in Table 1. The system is cooled down to T_{cool} = 300 K at a cooling time (τ) of 500 ps for all cases. The thickness in the build direction (z-axis) is varied starting from $10a$ lattice units to $192a$ keeping the transverse dimensions fixed at $16a \times 16a$. The layer thickness, layer-wise number of atoms, and the total number of atoms (at the end of the eighth layer) for some of the thickness cases are shown in Table 1.

Fig. 6 shows the FCC content in the cooled down layers (on the horizontal axis) for different melt thickness (vertical axis). We can see that the FCC fraction is converged at layer 4 to layer 5 for all the thicknesses studied. For lower melt thicknesses, we see single crystal growth with no significant defect structure. However, at higher thicknesses of added layers, a significant amount of defects emerges. A clear

Table 1
System parameters for different melt layer thickness studies.

System	Thickness (nm)	Atoms in the initial solid layer (L_0)	Atoms in each liquid layer	Maximum number of atoms simulated
$16a \times 16a \times 16a$	5.783	16,896	~14,221	132,088
$16a \times 16a \times 32a$	11.565	33,280	~28,284	261,663
$16a \times 16a \times 48a$	17.348	49,664	~42,702	395,008
$16a \times 16a \times 96a$	32.698	98,816	~86,462	776,986
$16a \times 16a \times 192a$	65.396	197,120	~172,597	1,554,385

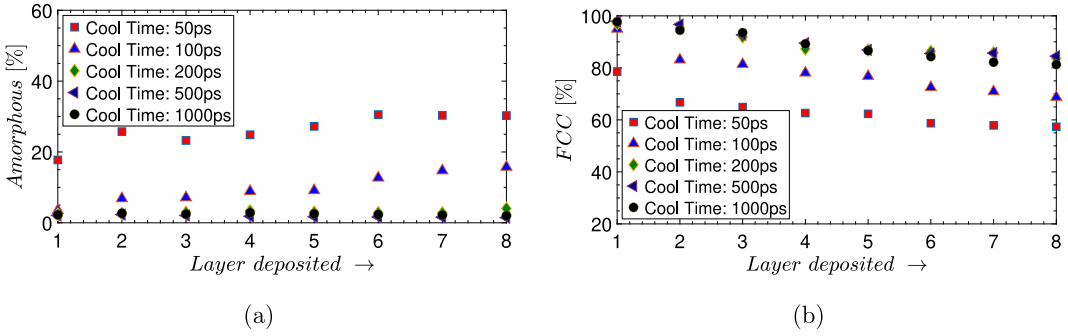

Fig. 5. Amorphous (a) and FCC (b) structure type evolution as a function of added layers for different cooling times in a $16a \times 16a \times 32a$ system.

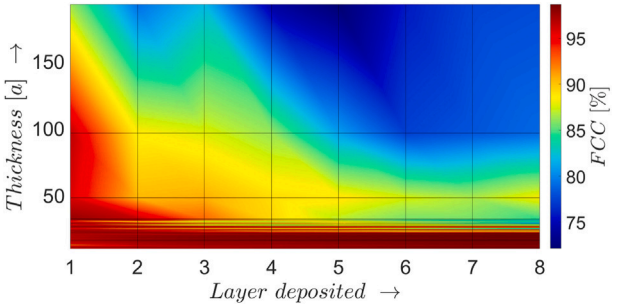

Fig. 6. Contour plot of FCC percentage as a function of layer thickness and the number of layers.

threshold thickness beyond which the trend of perfect crystallization changes to a defective structure is seen. For the case of Cu at 500 ps cooling time, this threshold value is estimated to be $24a \pm 2a$ (from 3 replica runs), at and beyond which the defect starts initiating and evolving with additional layers to the additive column.

Fig. 7 shows the defect structure at the end of the addition of layer number 8 for different thicknesses in the additive column. For the $16a$ thickness case, almost perfect crystallization is seen with a negligible fraction of stable dislocation loops. As the thickness of the molten layer is doubled to $32a$, grain boundaries emerge and a poly-crystal structure is seen, delineated by grain boundaries (identified as amorphous/white regions). The first grain contains vertical stacking faults while subsequent grains contain slanted twin boundaries or a combination of stacking faults and twin boundaries. The larger melt thickness simulated ($48a$) also forms larger grains, that initially contain amorphous regions of high dislocation densities, as seen in the last layer (Fig. 7(bottom)). These regions would subsequently reform during the addition of more layers to form smaller sub-grains. Overall, although different grain sizes are seen for $32a$ and $48a$ cases, the percentage of defects for these two cases are approximately similar.

The results seen here can be interpreted by studying the solidification kinetics in the melt. The solidification is primarily seen to proceed along two directions for an added molten layer as shown in Fig. 8 for the $96a$ thickness case. The molten layer in contact with the cooler substrate lattice has a fast solidification front that sweeps across the molten layer. The crystal orientation of the substrate is maintained in general. The solidification front at the top, in general, does not have the same crystal orientation as the substrate, and thus, when the two fronts interact, grain boundaries are formed.

For small layer thicknesses, defect-free single crystals are obtained as the faster solidification front reaches the top of the melt pool before the initiation or within the early stages of initiation of the slower front from the top. The critical layer thickness can be analytically found using the speeds of the solidification fronts as follows. The solidification speeds as measured from the case in Fig. 8 are tabulated in Table 2 (refer animation03 and animation04 in SI for layer-1 and layer-2, respectively). The solidification speed from a defect-free substrate is $v = 1.95$ Å/ps. The front speed at the top layer is much lower (0.494 Å/ps). The crystal structure for subsequent layers begins to form stable crystals only after a delay of $\tau \approx 40$ ps compared to the faster front. To identify the threshold thickness for achieving a single crystal, one needs to ensure that the fast solidification front reaches the top before the crystal (with a different orientation) has a chance to fully initiate at the top. This threshold thickness ($t_{critical}$) can be calculated as $t_{critical} = v\tau$ which is about $23a$, the threshold thickness as seen in Fig. 6 for the formation of defect-free single crystals. Fig. 7 shows the FCC distribution snapshot at the end of cooling of the 8th layer for $16a$ thickness case which demonstrates a single crystal structure below the threshold.

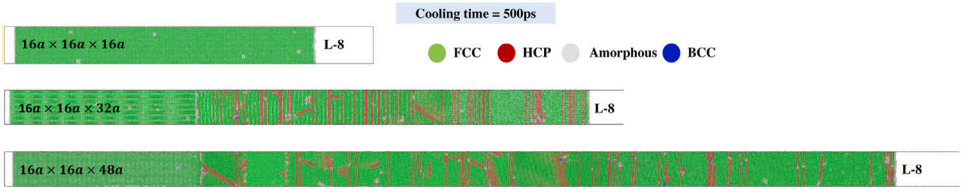

Fig. 7. Snapshot of the structures produced for three different deposited layer thicknesses at the end of deposition of eight layers.

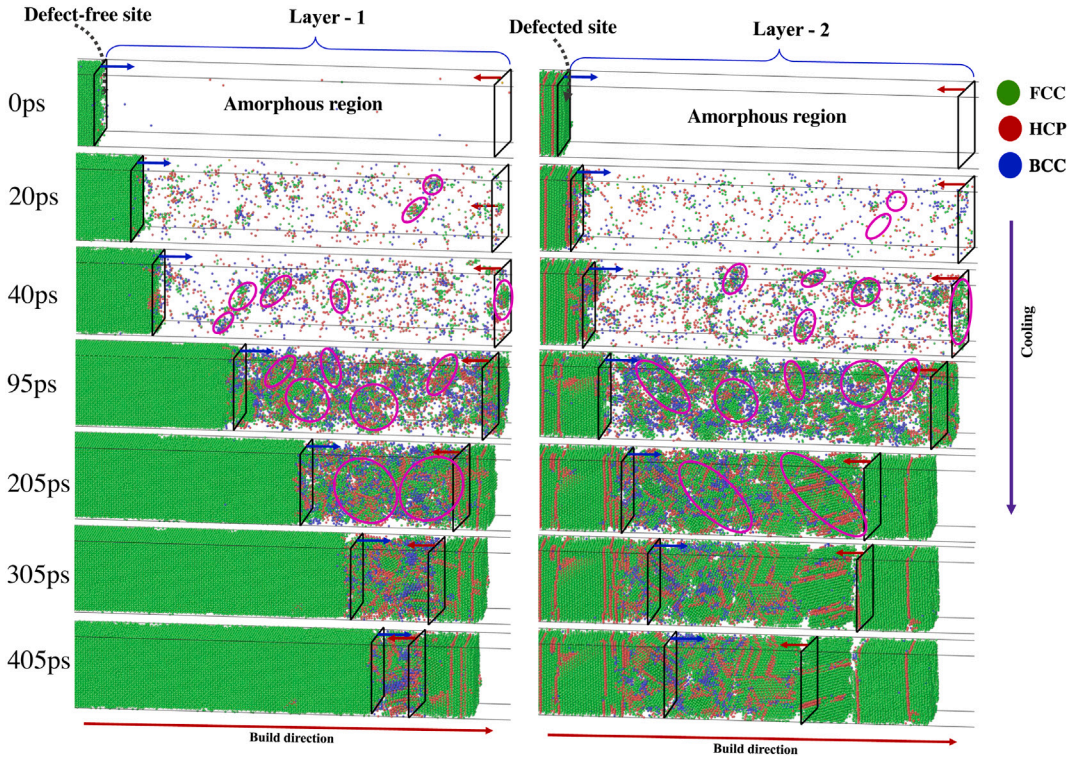

Fig. 8. Evolution of two solidification fronts demonstrating the cooling mechanism for a 96a thickness case for (left) layer-1 solidification with a perfectly crystalline substrate; and (right) layer-2 which nucleates from the defects left over at the top of layer-1.

Table 2
The value of solidification front speed at the bottom and top of the melt pool estimated for 96a thickness case.

Solidification front	$F^{crystal}_{bottom}$	F^{defect}_{bottom}	F^{free}_{top}
Solidification front speed [Å/ps]	1.95	0.768	0.494

Increasing the thickness of the melt beyond this critical thickness leads to an increase in the number of defects due to the interaction between two solidification fronts. The presence of defects on the substrate further slows down the primary solidification front. As seen in Fig. 8, if the substrate contains a large number of defect structures (layer 2 as shown at 0 ps), the solidification front velocity moves at a slower pace (v = 0.768 Å/ps compared to v = 1.95 Å/ps for solidification from a defect-free substrate). However, it is always faster than the solidification front that moves down from the top of the melt. This would mean that the solidification fronts meet roughly mid-way for layer 2 compared to layer 1 as seen in Fig. 8 and result in a grain boundary. The slower speed of the fronts from defective substrate also implies that it takes more time to achieve stable defect structures as the number of layers increase, a feature previously seen in Fig. 3.

In addition to the interaction between the two solidification fronts, each front interacts with homogeneous nuclei (shown as pink ellipsoids) formed within the melt as shown in Fig. 8. These nuclei when absorbed into the two larger solidification fronts leave defect remnants. For smaller thicknesses (e.g. 32a case shown in Fig. 7), these nuclei do not have time to grow as the solidification front rapidly covers the melt. However, the cases with larger thicknesses (e.g. 48a case shown in Fig. 7) have significantly large chunks of amorphous regions as the solidification fronts interact with larger and more differentiated internal nuclei that would take longer to coalesce into the primary crystallized region. These regions have higher interfacial energies that are relieved as the additive process proceeds through the formation of fine sub-grains.

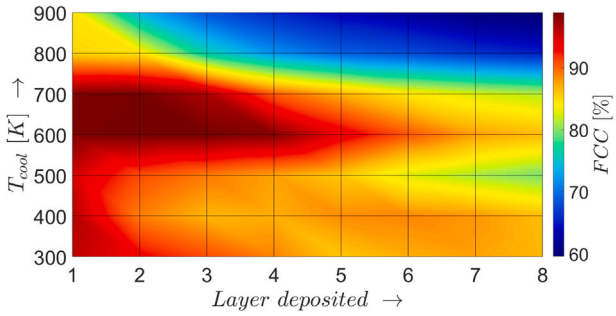

Fig. 9. FCC structure percentage obtained as a function of bed temperature and the number of layers deposited. A cooling time of 500 ps and a 48a layer thickness is used.

3.2. Effect of preheated beds (variation of parameter T_{cool})

In the study outlined in the previous section, each layer was cooled down to the room temperature T_{cool} = 300 K. Experimentally, it is known that preheating the powder beds to higher temperatures leads to fewer defects in the final product. For example, electron beam melted (EBM) parts have lower microcracks compared to selective laser melted (SLM) parts primarily owing to the lower cooling rate due to preheated powder beds and a vacuum chamber that dissipates heat away slower. In the molecular simulations, preheated beds can be simulated by increasing the parameter T_{cool}. For this section, we cool down each layer of the additive column to a temperature T_{cool} from 300 K to 900 K with an increment of 100 K. A layer thickness of 48a and cooling time of 500 ps are chosen for the simulations.

Fig. 9 plots the percentage of the FCC content for different layers as a function of T_{cool}. Starting from a higher defect content at 300 K, the defects initially improve as a function of temperature reaching almost a defect-free single crystal at 600 K and 700 K. As the temperature is further increased, defects again begin to increase significantly with

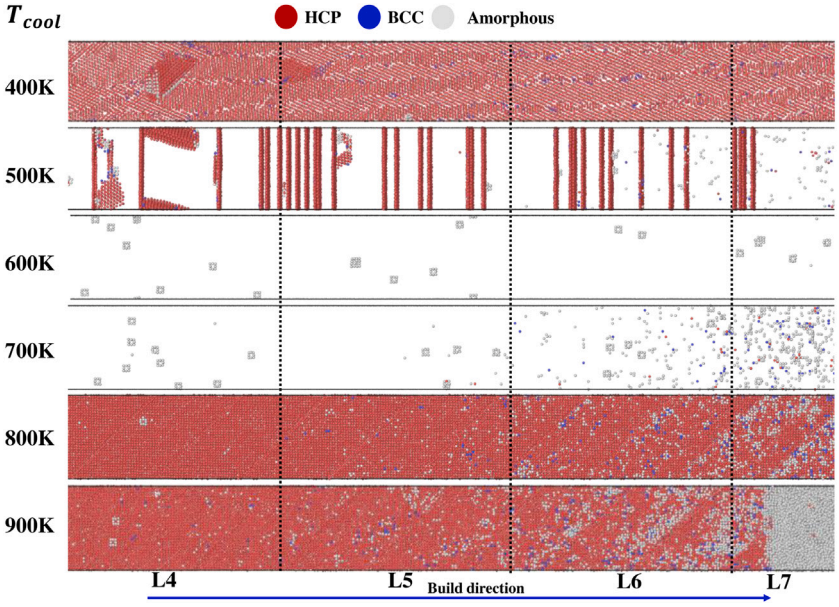

Fig. 10. Defect structure after cooling to different substrate temperatures (T_{cool}) (only 4 layers, i.e. $L_4 - L_7$ shown).

temperature. At higher bed temperatures, the temperature drop per unit time needed is lower for the same time of cooling which implies the slow cooling rates. Slow cooling rates are beneficial to reduce defects as the atoms have more time to rearrange and reduce defects as seen earlier in Fig. 5. On the contrary, there is an increase in defects beyond 600 K. This unusual behavior can be explained by looking at the defect structures formed at different cooling temperatures.

Fig. 10 shows the defect structure for various temperatures of the bed. Only the defects are shown in this figure (and the FCC structure is hidden). At 400 K and 500 K, most defects are of stacking fault type or grain and twin boundaries. At 600 K and 700 K all these defects are entirely removed. The most amorphous region pertains to the uncrystalized portion remained on the last layer. This is due to the fact that at higher cooling temperatures for this thickness system ($16a \times 16a \times 48a$), 500 ps of cool time is not enough for last layers as the column becomes larger. Therefore, as the temperature is further increased, the amorphous content significantly increases while a content of stacking faults remain similar to that of the lower temperatures. Fig. 11 shows the split between amorphous and HCP-type defects as a function of bed temperature for different layers. As seen in Fig. 11(a), the amorphous content begins to increase from 500 K, going toward the melting point of copper. At 900 K, as much as a third of the content is fully amorphous and no benefits of slow cooling rates are seen. Fig. 11(b) shows that the HCP content increases as the substrate's temperature is decreased below 600 K towards the room temperature. Thus, two mechanisms compete as the bed temperature is raised: (1) the slower cooling rates leading to lower stacking fault type defects and (2) high energy amorphous content as one goes closer to the melting point. The interaction between these mechanisms gives a sweet spot for the temperature of the preheated beds for copper at 600 K and 700 K.

3.3. Effect of inclusions

In this section, the effect of inclusions on atomistic scale defect evolution is studied. It is known that the use of high temperature stable, soft inclusions lead to improved toughness in the final structure, for example, multi-component oxide, oxy-sulfide or sulfide inclusions in iron welds [38]. Two types of inclusions are chosen in this study: a soft inclusion (silicon disulfide, having a melting point of 1363 K, and elastic modulus of 32 GPa) and a hard inclusion (silicon carbide, with the melting point of 3003 K, and elastic modulus of 323 GPa).

Table 3
Crystal properties of Al matrix, SiS_2 and SiC inclusions.

System	Structure	Elastic modulus	Melting point	Density at RT
Al [40]	FCC	70.2 GPa	933 K	2.70 gcm^{-3}
SiS_2 [41]	Tetragonal	32 GPa	1363 K	2.20 gcm^{-3}
SiC [41]	Cubic	323 GPa	3003 K	3.17 gcm^{-3}

To simulate inclusions in the melt, the melting point of the inclusions should be higher than the substrate such that the inclusion is retained in the melt. Because of the higher melting point of copper (1358 K), an Aluminum substrate (melting point of 933 K) was chosen for this example. The structure and density of the constituents are additionally listed in Table 3. The consistent valence force field (CVFF) [39] was used for the bonded interactions of SiS_2 and SiC inclusions. Aluminum lattice was modeled using the EAM potential as described in [37].

Leonard-Jones (LJ) potential [39] is used for non-bonded interaction of S-Al interaction for SiS_2 inclusion simulations. Al–SiC systems have been studied with Morse potential for interface fracture [42] and interface properties [43]. The Morse pairwise interactions energy is computed as follows:

$$E = D_o \left[e^{-2\alpha(r-r_o)} - 2e^{-\alpha(r-r_o)} \right] \qquad r < r_c \tag{2}$$

where, r is the distance between two particles, and the cut-off distance $r_c = 10$ Å. Other parameters for the Al–Si and Al–C non-bonded interactions using Morse potential, were originally obtained by Zhao et al. [44] and are summarized in Table 4. The LJ potential is similar in behavior to the Morse potential at the equilibrium distance but deviates as the distance between atoms gets shorter. Morse potential is primarily designed to avoid the singularity of the LJ potential as the interatomic distance goes to zero. This improves the system dynamics in cases where atomic collisions are expected, however, the equilibrium structure is expected to be similar.

First, the equilibrated density of pure Al at 1100 K is obtained by running NPT simulation at 1 bar pressure conditions and the density was observed to stabilize at $\rho_{liquid} = 2.297$ gcm^{-3}. Each layer of this melt density at 1100 K was added to the additive column. To insert the inclusion, atoms in the amorphous layer (with a volume equivalent to the volume and shape of the inclusion) are carved out by deletion from this melt pool layer. The melt with inclusion is again equilibrated at 1100 K at which point Aluminum melts while the inclusion is retained.

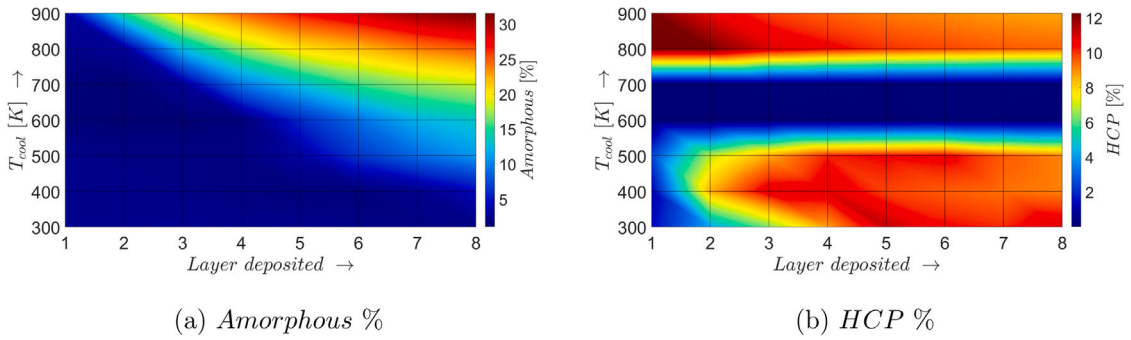

Fig. 11. Defect evolution in the additive column under different substrate temperatures with an increase in the number of layers depicting (a) percentage of amorphous regions and (b) percentage of HCP regions.

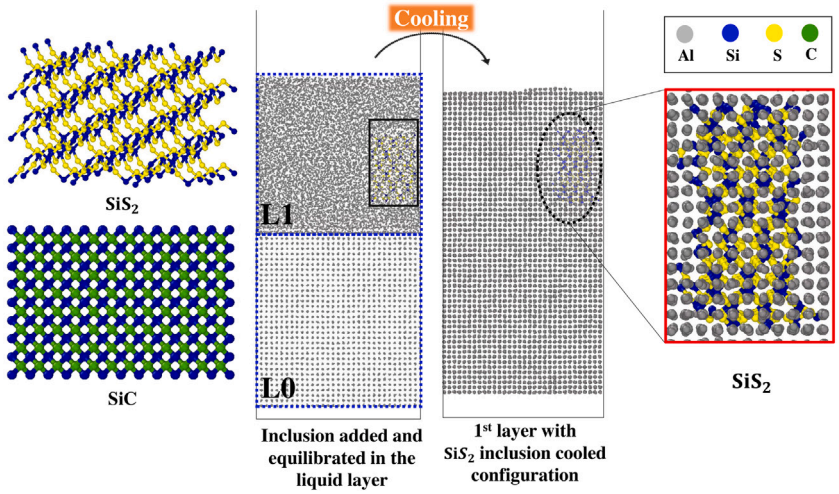

Fig. 12. (left) Inclusion SiS_2 and SiC (right) SiS_2 as solidified in first layer of Al matrix after cooling down ($V_f = 2.76\%$ for SiS_2 and $V_f = 2.88\%$ for SiC).

Table 4
Values of the Morse potential parameters obtained by applying an inverse method to *ab initio* data [44].

Pair	Parameter	Value
Al–Si	D_o	0.4824 eV
	α	1.322 Å^{-1}
	r_o	2.92 Å
Al–C	D_o	0.4691 eV
	α	1.738 Å^{-1}
	r_o	2.246 Å

The same process as explained in the 'methods' section is repeated for modeling sequential addition of the melt. The system is cooled to room temperature with a cooling time of 100 ps. An Al $16a \times 16a \times 16a$ thickness system is chosen for this study and a single inclusion is added at each layer. Fig. 12 depicts the inclusions SiS_2 and SiC in the first layer of solidified Al melt after cooling down. Volume fractions of the inclusion for the two cases studied are similar with $V_f = 2.76\%$ for SiS_2 and $V_f = 2.88\%$ for SiC inclusion.

Fig. 13(a) shows the influence of the soft (SiS_2) and the hard (SiC) inclusion on defect evolution as compared to a process with pure Al. The soft inclusion showed the lowest defect percentage and the hard inclusion showed a significant amount of defects. Fig. 13(b) depicts the defect structure after the sixth melt layer is cooled. Pure Al forms a polycrystalline structure with grain boundaries (amorphous vertical regions) under these conditions with a few retained stacking faults. The soft inclusion results in retention of the single crystal orientation and the stacking faults are eliminated.

Solidification velocities of the pure Al and Al with SiS_2 are found to be similar, showing that the SiS_2 inclusion does not inhibit or enhance solidification front speeds. However, it partially shields interaction between the competing solidification fronts. On the other hand, solidification fronts move much slower in the case of a harder SiC inclusion. In this case, large amorphous regions are formed around the precipitate. This amorphous region is seen at layers 5 and 6 in Fig. 13(b) (bottom) but also formed when layers 1 to 4 were added. These regions subsequently reformed to a twinned region emanating from the precipitate (as seen in layers 2–4). Due to the lack of defects, the use of softer inclusions in metal powders is worth pursuing in the future to achieve products with improved fracture properties.

4. Conclusions

In this work, we use molecular dynamics simulations to systematically model a nanoscale additive column to investigate the influence of layer thickness, cooling time, target cooling temperature and alloy inclusions on the final defect structure. Such simulations, although idealizing a very complex additive manufacturing process, can capture the non-equilibrium physics at the nanoscale that leads to the formation of defect structures. It is found that the percentage of the defect-free content of copper converges when a sufficient number of layers are added. The solidification is primarily seen to proceed along two directions for an added molten layer. The molten layer in contact with the cooler lattice has a fast solidification front that competes with the slower solidification front starting from the top of the melt layer. The defect structure formed strongly depends on the interactions between these competing solidification fronts. The key takeaways from these simulations are as follows:

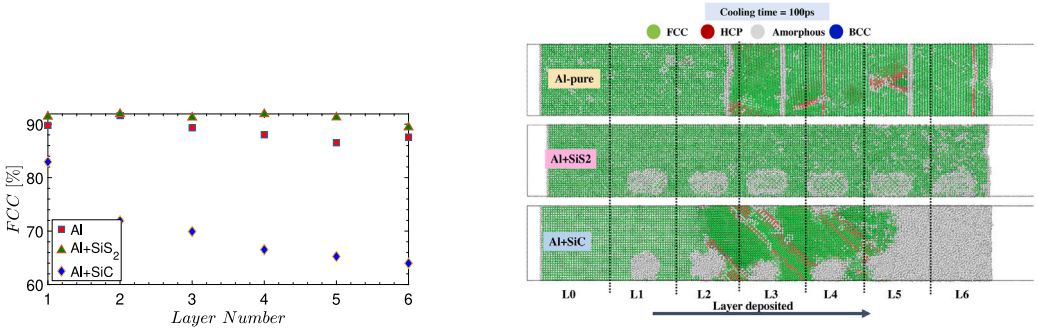

(a) FCC % (b) CNA snapshots

Fig. 13. (a) FCC percentage evolution as a function of the deposited number of layers for pure Al compared against Al with two inclusions studied here and (b) defect snapshots after deposition of six layers for $16a$ layer thickness.

- A lower cooling rate leads to a reduction in defects, however, the benefits diminish below a critical rate as stable dislocation defects form that cannot be further eliminated.
- Up to a critical layer thickness, the defect-free single crystals are obtained as the faster solidification front reaches the top of the melt pool before the stable formation of the slower front from the top.
- As the thickness of the molten layer increases beyond a critical thickness, grain boundaries emerge and a polycrystalline structure is formed. The grain sizes typically increase with the layer thickness. However, for the large melt thicknesses, the amorphous regions of high dislocation densities are formed as the solidification fronts interact with more differentiated homogeneous nuclei. These regions subsequently reform to create smaller sub-grains.
- The defect content can be significantly reduced by raising the temperature of the powder bed to a critical temperature. At low bed temperatures, the faster cooling rates lead to significant dislocation defects. At higher temperatures, the cooling rates are lower leading to a lower dislocation content. However, higher temperatures also lead to an increase in amorphous content. There is a critical value of temperature that balances both the dislocation defects and the amorphous content.
- Finally, the effect of added soft inclusion (SiS_2) and a hard inclusion (SiC) on the defect structure in Aluminum is studied. SiC inclusion significantly slows down the solidification front leading to retained defect structure. However, the addition of SiS_2 does not modify the solidification velocity compared to pure Al. Additionally, the presence of SiS_2 is seen to reduce defect content compared to the pure metal.

The presented results are an initial step towards a computational understanding of the additive process parameter–crystal structure relationship in a non-equilibrium setting. This study can be improved by considering the effect of actual laser heating profiles, surface cooling in a non-vacuum environment, and the interaction of melt pools. The methodology can also be used to model the evolution of residual stresses in the unit cell as a function of process parameters and simulate the stress–strain response after processing. A critical advantage of a first principle approach is that the simulations can be used to perform alloy design, as the preliminary inclusion case presented here, but with improved modeling of formation and dispersion of multiple inclusions.

CRediT authorship contribution statement

Gurmeet Singh: Conceptualization, Investigation, Methodology, Supervision, Formal analysis, Validation, Visualization, Writing – original draft, Writing – review & editing. **Anthony M. Waas:** Conceptualization, Investigation, Supervision, Project administration, Writing – review & editing. **Veera Sundararaghavan:** Conceptualization, Formal analysis, Investigation, Methodology, Supervision, Project administration, Writing – review & editing.

Declaration of competing interest

The authors declare that they have no known competing financial interests or personal relationships that could have appeared to influence the work reported in this paper.

Data availability statement

The data that support the findings of this study are available from the corresponding author upon reasonable request.

Acknowledgments

This research was supported in part through computational resources and services provided by Advanced Research Computing at the University of Michigan, Ann Arbor. The authors would like to thank Mr. Aaditya Lakshmanan for his valuable discussions.

Appendix A. Supplementary data

Supplementary material related to this article can be found online at https://doi.org/10.1016/j.commatsci.2021.110807. Supplementary material contains animations of the simulations of the additive column crystallization and the defect structure evolution during the cooling of different layers under various conditions.

References

[1] Lawrence E Murr, Sara M Gaytan, Diana A Ramirez, Edwin Martinez, Jennifer Hernandez, Krista N Amato, Patrick W Shindo, Francisco R Medina, Ryan B Wicker, Metal fabrication by additive manufacturing using laser and electron beam melting technologies, J. Mater. Sci. Technol. 28 (1) (2012) 1–14.
[2] Dirk Herzog, Vanessa Seyda, Eric Wycisk, Claus Emmelmann, Additive manufacturing of metals, Acta Mater. 117 (2016) 371–392.
[3] Amit Bandyopadhyay, Yanning Zhang, Susmita Bose, Recent developments in metal additive manufacturing, Curr. Opin. Chem. Eng. 28 (2020) 96–104.
[4] Chi Zhang, Fei Chen, Zhifeng Huang, Mingyong Jia, Guiyi Chen, Yongqiang Ye, Yaojun Lin, Wei Liu, Bingqing Chen, Qiang Shen, Lianmeng Zhang, Enrique J. Lavernia, Additive manufacturing of functionally graded materials: A review, Mater. Sci. Eng. A 764 (2019) 138209.
[5] Raeann VanSickle, David Foehring, Huck Beng Chew, John Lambros, Microstructure effects on fatigue crack growth in additively manufactured Ti–6Al–4V, Mater. Sci. Eng. A 795 (2020) 139993.
[6] P. Bajaj, A. Hariharan, A. Kini, P. Kürnsteiner, D. Raabe, E.A. Jägle, Steels in additive manufacturing: A review of their microstructure and properties, Mater. Sci. Eng. A 772 (2020) 138633.
[7] Nima Shamsaei, Aref Yadollahi, Linkan Bian, Scott M Thompson, An overview of direct laser deposition for additive manufacturing; Part II: Mechanical behavior, process parameter optimization and control, Addit. Manuf. 8 (2015) 12–35.
[8] Jamison L. Bartlett, Xiaodong Li, An overview of residual stresses in metal powder bed fusion, Addit. Manuf. 27 (2019) 131–149.

[9] Liang Wang, Sergio D. Felicelli, James E. Craig, Experimental and numerical study of the LENS rapid fabrication process, Trans. ASME, J. Manuf. Sci. Eng. 131 (4) (2009) 0410191–0410198.
[10] Liang Wang, Sergio D. Felicelli, Phillip Pratt, Residual stresses in LENS-deposited AISI 410 stainless steel plates, Mater. Sci. Eng. A 496 (1–2) (2008) 234–241.
[11] Jinghao Li, Xianglin Zhou, Mathieu Brochu, Nikolas Provatas, Yaoyao Fiona Zhao, Solidification microstructure simulation of Ti-6Al-4V in metal additive manufacturing: A review, Addit. Manuf. 31 (2020) 100989.
[12] Scott M Thompson, Linkan Bian, Nima Shamsaei, Aref Yadollahi, An overview of direct laser deposition for additive manufacturing; Part I: Transport phenomena, modeling and diagnostics, Addit. Manuf. 8 (2015) 36–62.
[13] Shijia Chen, Gildas Guillemot, Charles André Gandin, Three-dimensional cellular automaton-finite element modeling of solidification grain structures for arc-welding processes, Acta Mater. 115 (2016) 448–467.
[14] Xuxiao Li, Wenda Tan, Numerical investigation of effects of nucleation mechanisms on grain structure in metal additive manufacturing, Comput. Mater. Sci. 153 (2018) 159–169.
[15] O. Zinovieva, A. Zinoviev, V. Ploshikhin, Three-dimensional modeling of the microstructure evolution during metal additive manufacturing, Comput. Mater. Sci. 141 (2018) 207–220.
[16] P Prabhakar, William J Sames, R Dehoff, Sudarsanam Suresh Babu, Computational modeling of residual stress formation during the electron beam melting process for Inconel 718, Addit. Manuf. 7 (2015) 83–91.
[17] Seshadev Sahoo, Kevin Chou, Phase-field simulation of microstructure evolution of Ti-6Al-4V in electron beam additive manufacturing process, Addit. Manuf. 9 (2016) 14–24.
[18] Joel Heang Kuan Tan, Swee Leong Sing, Wai Yee Yeong, Microstructure modelling for metallic additive manufacturing: A review, Virtual Phys. Prototyp. 15 (1) (2020) 87–105.
[19] A.V. Karavaev, V.V. Dremov, T.A. Pravishkina, Precise calculation of melting curves by molecular dynamics, Comput. Mater. Sci. 124 (2016) 335–343.
[20] Ebrahim Asadi, Mohsen Asle Zaeem, Sasan Nouranian, Michael I. Baskes, Two-phase solid-liquid coexistence of Ni, Cu, and Al by molecular dynamics simulations using the modified embedded-atom method, Acta Mater. 86 (2015) 169–181.
[21] Xiaoxiao Sui, Yongjian Cheng, Naigen Zhou, Binbing Tang, Lang Zhou, Molecular dynamics simulation of the solidification process of multicrystalline silicon from homogeneous nucleation to grain coarsening, CrystEngComm 20 (25) (2018) 3569–3580.
[22] Avik Mahata, Mohsen Asle Zaeem, Evolution of solidification defects in deformation of nano-polycrystalline aluminum, Comput. Mater. Sci. 163 (2019) 176–185.
[23] Yasushi Shibuta, Toshio Suzuki, A molecular dynamics study of cooling rate during solidification of metal nanoparticles, Chem. Phys. Lett. 502 (1–3) (2011) 82–86.
[24] H.Y. Zhang, F. Liu, Y. Yang, D.Y. Sun, The molecular dynamics study of vacancy formation during solidification of pure metals, Sci. Rep. 7 (1) (2017) 1–8.
[25] Sachin Kurian, Reza Mirzaeifar, Selective laser melting of aluminum nano-powder particles, a molecular dynamics study, Addit. Manuf. 35 (2020) 101272.
[26] Qi Jiang, Haishun Liu, Jinyan Li, Dengfeng Yang, Yue Zhang, Weiming Yang, Atomic-level understanding of crystallization in the selective laser melting of Fe50Ni50 amorphous alloy, Addit. Manuf. 34 (2020) 101369.
[27] Xiaohua Hu, Andrzej Nycz, Yousub Lee, Benjamin Shassere, Srdjan Simunovic, Mark Noakes, Yang Ren, Xin Sun, Towards an integrated experimental and computational framework for large-scale metal additive manufacturing, Mater. Sci. Eng. A 761 (2019) 138057.
[28] Guanghua Sui, Ming C. Leu, Investigation of layer thickness and surface roughness in rapid freeze prototyping, J. Manuf. Sci. Eng. 125 (3) (2003) 556–563.
[29] A.V. Müller, G. Schlick, R. Neu, C. Anstätt, T. Klimkait, J. Lee, B. Pascher, M. Schmitt, C. Seidel, Additive manufacturing of pure tungsten by means of selective laser beam melting with substrate preheating temperatures up to 1000 C, Nucl. Mater. Energy 19 (2019) 184–188.
[30] Steve Plimpton, Fast parallel algorithms for short-range molecular dynamics, J. Comput. Phys. 117 (1) (1995) 1–19.
[31] Hans C. Andersen, Molecular dynamics simulations at constant pressure and/or temperature, J. Chem. Phys. 72 (4) (1980) 2384–2393.
[32] Alex A. Samoletov, Carl P. Dettmann, Mark A.J. Chaplain, Thermostats for "slow" configurational modes, J. Stat. Phys. 128 (6) (2007) 1321–1336.
[33] Peter Mahler Larsen, Søren Schmidt, Jakob Schiøtz, Robust structural identification via polyhedral template matching, Modelling Simulation Mater. Sci. Eng. 24 (5) (2016) 055007.
[34] Alexander Stukowski, Visualization and analysis of atomistic simulation data with OVITO–the open visualization tool, Modelling Simulation Mater. Sci. Eng. 18 (1) (2009) 015012.
[35] Alexander Stukowski, Structure identification methods for atomistic simulations of crystalline materials, Modelling Simulation Mater. Sci. Eng. 20 (4) (2012) 045021.
[36] Daniel Faken, Hannes Jónsson, Systematic analysis of local atomic structure combined with 3D computer graphics, Comput. Mater. Sci. 2 (2) (1994) 279–286.
[37] X.W. Zhou, R.A. Johnson, HNG Wadley, Misfit-energy-increasing dislocations in vapor-deposited CoFe/NiFe multilayers, Phys. Rev. B 69 (14) (2004) 144113.
[38] T. Koseki, G. Thewlis, Overview inclusion assisted microstructure control in C–Mn and low alloy steel welds, Mater. Sci. Technol. 21 (8) (2005) 867–879.
[39] Pnina Dauber -Osguthorpe, Victoria A Roberts, David J Osguthorpe, Jon Wolff, Moniqe Genest, Arnold T Hagler, Structure and energetics of ligand binding to proteins: Escherichia coli dihydrofolate reductase-trimethoprim, a drug-receptor system, Protein. Struct. Funct. Bioinform. 4 (1) (1988) 31–47.
[40] G.V. Sin'Ko, N.A. Smirnov, Ab initio calculations of elastic constants and thermodynamic properties of bcc, fcc, and hcp Al crystals under pressure, J. Phys.: Condens. Matter 14 (29) (2002) 6989.
[41] Maarten De Jong, Wei Chen, Thomas Angsten, Anubhav Jain, Randy Notestine, Anthony Gamst, Marcel Sluiter, Chaitanya Krishna Ande, Sybrand Van Der Zwaag, Jose J Plata, et al., Charting the complete elastic properties of inorganic crystalline compounds, Sci. Data 2 (1) (2015) 1–13.
[42] Chinmaya R. Dandekar, Yung C. Shin, Molecular dynamics based cohesive zone law for describing Al-SiC interface mechanics, Composites A 42 (4) (2011) 355–363.
[43] Xuan Luo, Gefei Qian, E.G. Wang, Changfeng Chen, Molecular-dynamics simulation of Al/SiC interface structures, Phys. Rev. B 59 (15) (1999) 10125.
[44] Hanyue Zhao, Nanxian Chen, An inverse adhesion problem for extracting interfacial pair potentials for the Al(0 0 1)/3C-SiC(0 0 1) interface, Inverse Problems 24 (3) (2008) 035019.